Supporting Information

Controllable amorphization and morphology engineering on mixed-valence MOFs for ultra-fast and high-stability near-pseudocapacitance Li^+ storage

Junjie Yu, ‡ [a] Yan Wu, ‡ [a] Tianlang Peng, [a] Qi Qi, [a] Xinyu Ma, [a] Yafei Gu, [a] Xinguang Li, [a] Jianshen Ding, [a] Shiang Chen, [a] Xiaoshi Hu, *[a] Yanling Wang, [b] Qinqin Xiong, [a] Yongjun Yuan [a] and Haiying Qin [a]

a Key Laboratory of Novel Materials for Sensor of Zhejiang Province and New Energy Materials Research Center, College of Materials and Environmental Engineering, Hangzhou Dianzi University, Hangzhou, 310018, PR China

b College of Information Engineering, Zhejiang University of Water Resources and Electric Power, Hangzhou, 310018, PR China

‡ J. Yu and Y. Wu contributed equally to this work.

*Email: xshu@hdu.edu.cn

Experimental details

Synthesis of Fe-based MOFs: In a typical synthesis of the series of Fe (II, III)-MOFs materials, 27.5 mol L^{-1} of $FeCl_2$·4 H2O, 11.3 mmol L^{-1} of 2,5-dihydroxy terephthalic acid were dissolved in a 80/60/40/20 mL mixed solvent (dimethyl formamide/methanol/deionized water = 18 : 1 : 1, v : v : v) in a beaker sealed in plastic wrap. Then, the transparent mixed solution was poured into a 100 mL Teflon-lined stainless steel autoclave and placed in an oven at 115 ℃ for 18 h. After the autoclave was cooled down naturally in the fumehood, the resultant powder was collected by filtration, washed with DMF, H_2O and MeOH for several times. The yellow product of the series of Fe (II, III)-MOFs was obtained after drying in a vacuum oven at about 100 ℃ for 6 h and named as Fe (II, III)-MOFs-80, Fe (II, III)-MOFs-60, Fe (II, III)-MOFs-40, and Fe (II, III)-MOFs-20, respectively, according to the solution volume used. For the control experiment of the synthesis of $FeCl_3$-MOF-20, the precursor salts of $FeCl_2$·4 H_2O was replaced by $FeCl_3$·6 H_2O with other experiment parameters kept constant as that of Fe (II, III)-MOFs-20 sample.

Materials Characterization: The structural and composition information was determined using X-ray diffraction (PXRD, MiniFlex 300/600) with the Cu−Kα radiation (λ=1.54056 Å) in a 2θ range of 5°–90° at a scan speed of 10° min^{-1}. Surface elemental composition and valence state were measured by X-ray photoelectron spectroscopy (XPS) tests performed on a Thermo ESCALAB 250XI spectrometer. The external morphologies and internal structures of material could be observed by field-emission scanning electron microscopy (SEM, JAPAN S-4800, HITACHI) and transmission electron microscopy (TEM: JEM-2100F, JEOL). SEM mapping and HRTEM, SAED were also carried out on S-4800 and JEM-2100F, respectively. The surface area and porosity were measured by a nitrogen adsorption analyzer (ASAP 2020, Micromeritics, USA) after degassing the sample over 150 °C. Fourier-transform infrared spectroscopy (FT-IR) spectra were performed on Nicolet-Nexus 670 spectrometer within the wavenumber ranging from 400 to 4000 cm^{-1}. The thermal stability was studied by thermogravimetric analysis (TGA) (NETZSCH TG 209 F1 Libra) in air flow at a heating rate of 10 °C min^{-1} from 30 °C to 800 °C.

Electrochemical measurements: The working electrodes were prepared according to an aqueous slurry coating approach: a homogeneous mixture of active material, conductive Super P and sodium carboxymethyl cellulose binder (CMC) binder in a weight ratio of 70 : 20 : 10 with distilled water as the solvent was uniformly blade-coated onto the copper foil, dried in a vacuum at 110 °C overnight, and then cut into circular electrodes. The active material mass loading in the electrode was around 0.7-1.5 mg cm^{-2}. After that, the prepared anode, a Celgard separator, pure Li counter electrode, electrolyte of $LiPF_6$ (1 M) in ethyl methyl carbonate/ethylene carbonate/dimethyl carbonate (1:1:1 vol.%) with 5 vol.% fluoroethylene carbonate, and the other components of the coin-type cell were assembled into CR2032-type half cells in an Ar-filled glove box (H_2O < 0.1 ppm, O_2 < 0.1 ppm). The assembled coin-type cells were aged for at least 12 h before electrochemical test. All the specific capacities were calculated based on the total mass of Fe MOF materials. Cyclic voltammetry (CV) was performed on an electrochemical workstation (Autolab PGSTAT302N) between the voltage ranges of 0.005-3 V. Electrochemical impedance spectroscopy (EIS) measurements were also performed on an electrochemical workstation (Autolab PGSTAT302N) with the frequency range of 10^5 Hz to 10^{-2} Hz. Galvanostatic charge-discharge measurements were carried out on a battery tester (LAND CT2001A) in the voltage range of 0.01–3.00 V (vs. Li^+/Li).

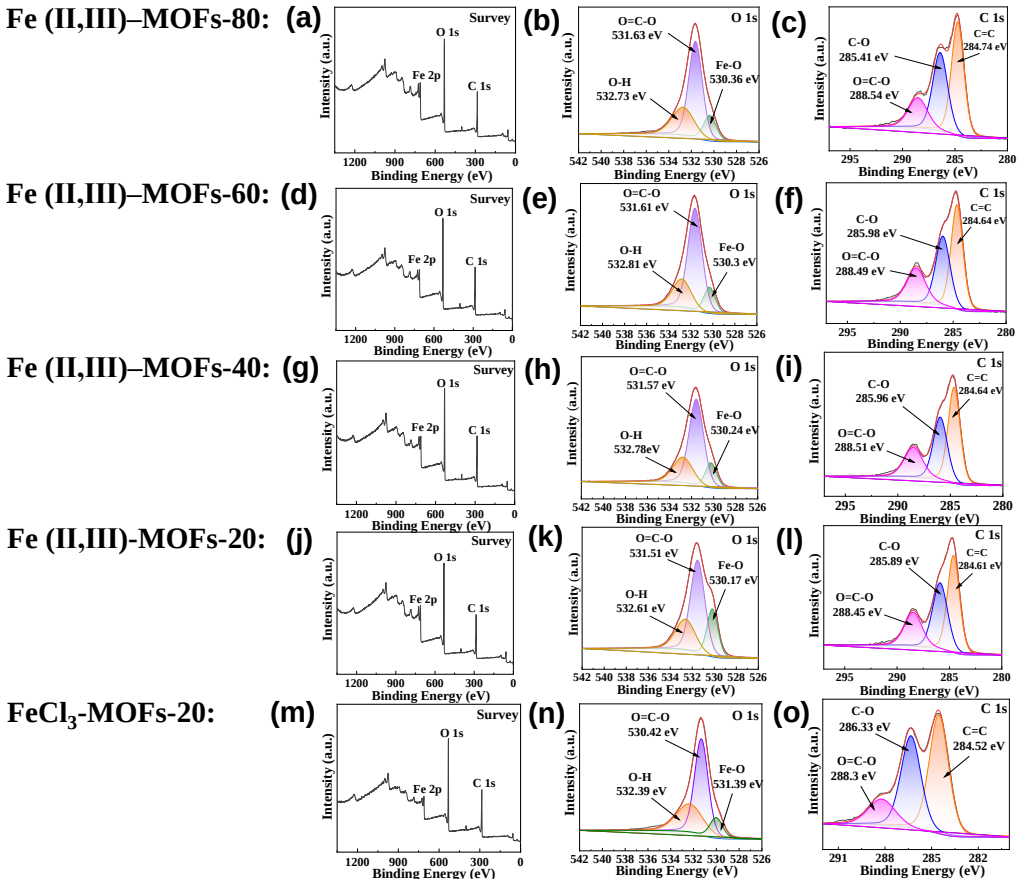

Fig. S1 (a, d, g, j, m) Survey spectrum, (b, e, h, k, n) High-resolution spectra for O 1S, and (c, f,i, l, o) High-resolution spectra for C 1S of the obtained four Fe (II, III)-MOFs and $FeCl_3$-MOF-20 control sample. The full-survey-scan spectrum of the Fe-MOFs (Fig. S1 (a, d, g, j, m)) showed peaks for Fe, O, C elements at their respective binging energy. The deconvoluted O 1S spectra (Fig. S1 (b, e, h, k, n)) was divided into three peaks at 532.29-532.81 eV, 530.42-531.63 eV and 530.17-531.39 eV, respectively related to oxygen in adsorbed H_2O, O=C-O on the carboxylate groups, and Fe-O, proving the successful fabrication of these Fe-based MOFs.[1] In the deconvoluted C 1S spectra (Fig. S1 (c, f, i, l, o)), the three peaks at 288.3-288.54 eV, 285.41-286.33 eV, 284.52-284.74 eV could be assigned to carbon in C=O-O, C-O, and C=C of the dhtp ligand, respectively.[1] It can be also found that the as-produced four Fe (II, III)-MOFs and $FeCl_3$-MOF-20 show the similar coordination structure between metal Fe ions and dhtp ligand.

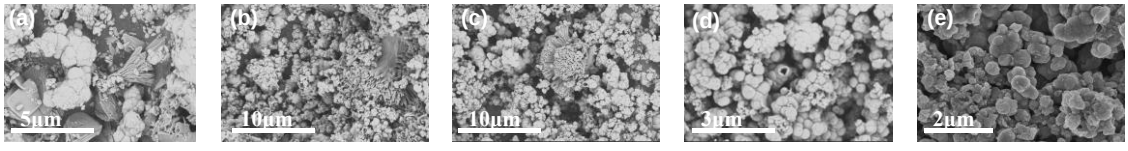

Fig. S2 SEM images of (a) Fe (II, III)-MOFs-80, (b) Fe (II, III)-MOFs-60, (c) Fe (II, III)-MOFs-40, (d) Fe (II, III)-MOFs-20 and (e) $FeCl_3$-MOF-20.

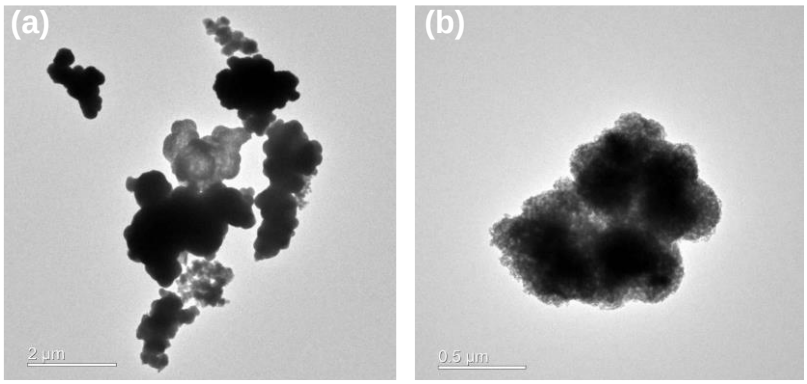

Fig. S3 TEM images of $FeCl_3$-MOF-20.

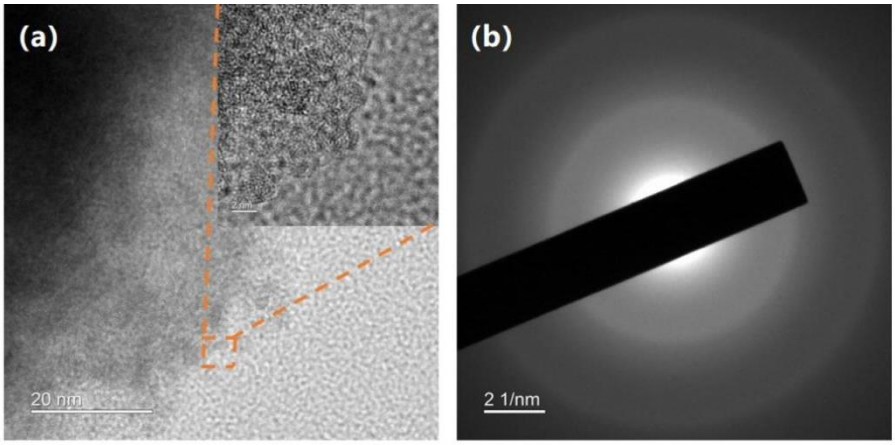

Fig. S4 (a) HRTEM micrograph and (b) corresponding SAED pattern of amorphous Fe (II, III)-MOFs-20. The absence of lattice fringe and weak amorphous halo are shown.

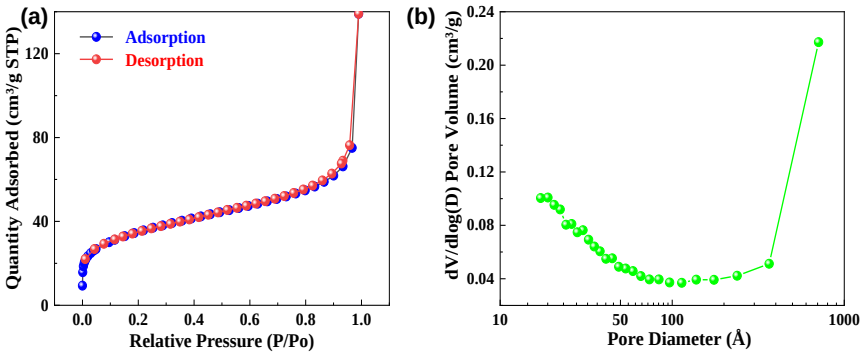

Fig. S5 (a) N_2 adsorption/desorption isotherms and (b) associated BJH pore size distribution of $FeCl_3$-MOF-20. The N_2 adsorption-desorption and corresponding BJH curves exhibit the characteristics of mesoporous materials. The specific surface area was calculated to be only 121.5 $m^2 g^{-1}$, including t-Plot micropore area of 24.0 $m^2 g^{-1}$, suggesting low MOF porosity of the amorphous $FeCl_3$-MOF-20 nanomaterials.

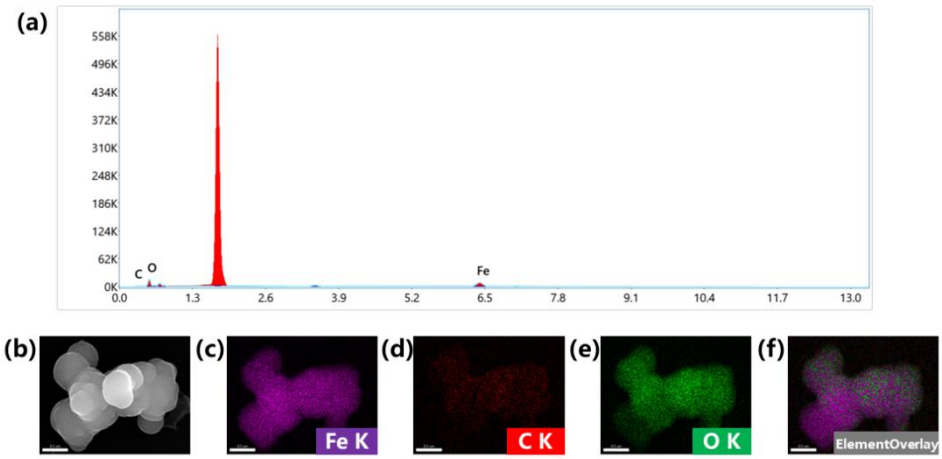

Fig. S6 (a) SEM-EDS spectrum and (b-f) corresponding elemental mapping images from selected region in SEM. The SEM-EDS analysis clearly reveals the coexistence and homogenous distribution of expected Fe, C, and O elements within the spheres, further demonstrating its uniform composition and the pure phase result draw by XRD (Fig. 2a).

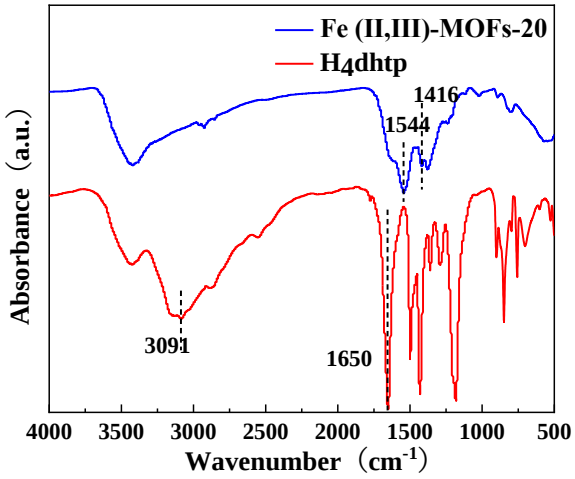

Fig. S7 FT-IR spectra of Fe (II, III)-MOFs-20 and H_4dhtp power. It was observed that characteristic absorption peaks of the nonionized 2,5-dihydroxy terephthalic acid (ν_{O-H}, 3091 cm^{-1}; $\nu_{C=O}$, 1650 cm^{-1}) are not present in Fe (II, III)-MOFs-20, while new absorption peaks which are associated with the asymmetric and symmetric stretching vibrations of carboxylate groups, arise at 1544 cm^{-1} and 1416 cm^{-1}, respectively.[2] This result suggested that Fe (II)/Fe (III) ions have been coordinated with the 2,5-dihydroxy terephthalic acid ligand.

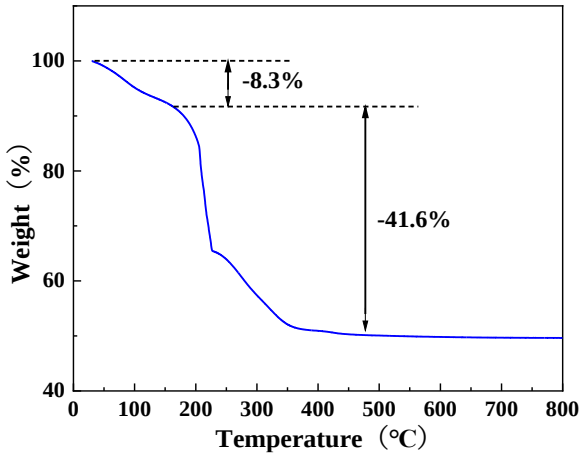

Fig. S8 TG behavior of Fe (II, III)-MOFs-20. It is obvious that the Fe (II, III)-MOFs-20 MOF experiences a slight weight-loss step (8.3%) below 150 ℃, which results from the loss of physisorbed water molecules. As the temperature further rises, the sample further experiences an obvious weight-loss step (41.6%) from 150 ℃ to 400 ℃, which is associated with the decomposition of MOF skeleton.

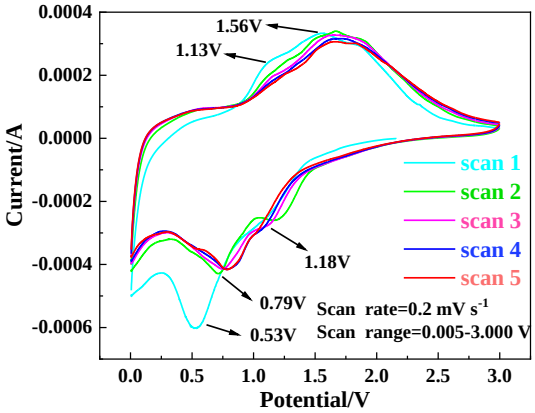

Fig. S9 CV curves of the Fe (II, III)-MOFs-20 electrode at a scan rate of 0.2 mV s^{-1} in the voltage window of 0.005 V-3.0 V vs Li/Li^{+}. The CV curves for the Fe (II, III)-MOFs-20 electrode exhibit with two pairs of well-defined cathodic/anodic peaks and the curves show good superposition in the consecutive scans, which is consistent with galvanostatic charge-discharge curves.

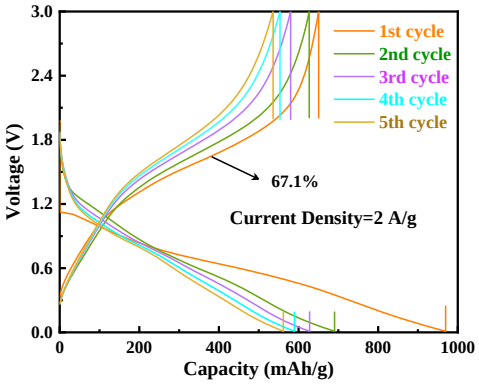

Fig. S10 Galvanostatic charge–discharge profiles of Fe (II, III)-MOFs-20 anode at 2A g^{-1}.

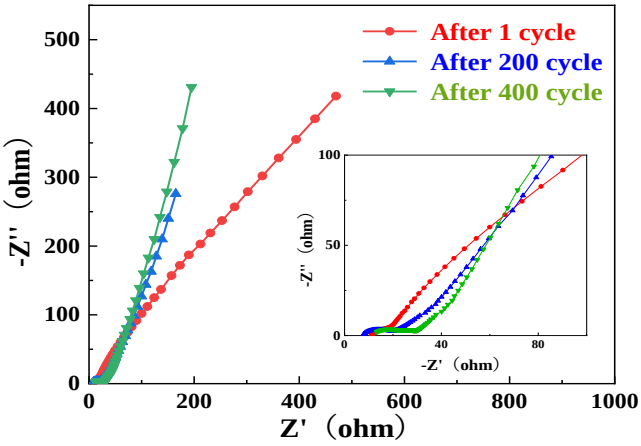

Fig. S11 EIS spectra for Fe (II, III)-MOFs-20 at 1st/200th/400th cycles with a current density of 1000 mA g^{-1}. It is clear that both the impedance associated charge-transfer resistance (R_{ct}, semicircle across the medium-frequency range) and the SEI film resistance (R_{SEI}, semicircle across the high-frequency range) in Fe (II, III)-MOFs-20 are low during cycling, which demonstrates good conductive capability of the Fe (II, III)-MOFs-20 electrode and limited SEI layer growth during cycling, leading to excellent rate capability and superior cyclability.

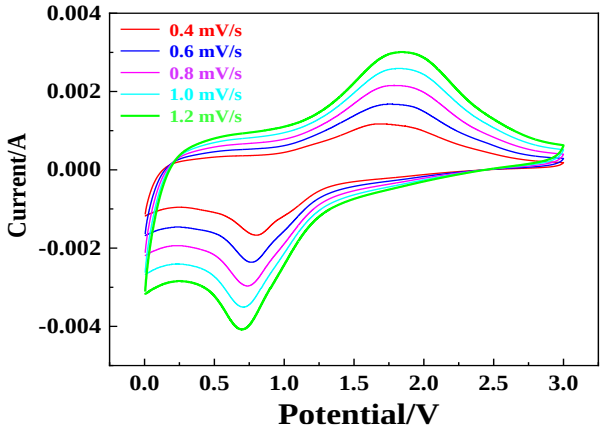

Fig. S12 CV curves at different scan rates of the Fe (II, III)-MOFs-20 electrode after several cycles.

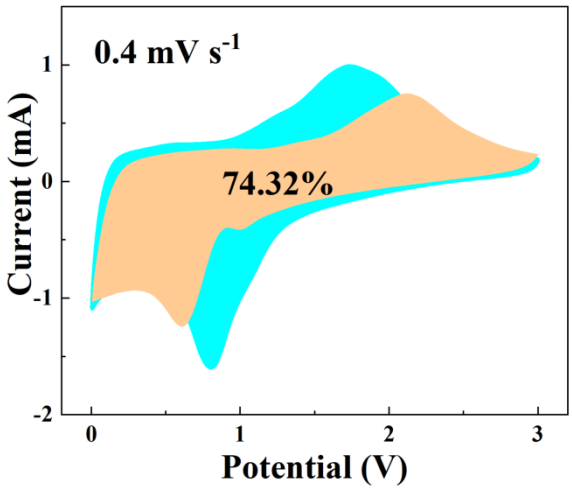

Fig. S13 Pseudocapacitive current (orange region) with respect to the total current for Fe (II, III)-MOFs-20 electrode at 0.4 mV s^{-1}.

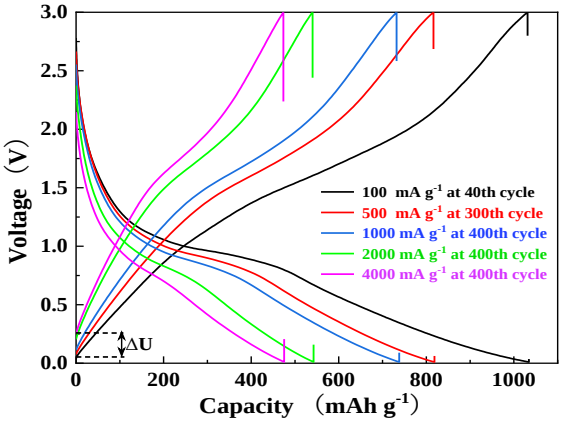

Fig. S14 The charge-discharge curves of Fe (II, III)-MOFs-20 anode at different current density after the cycling test.

.

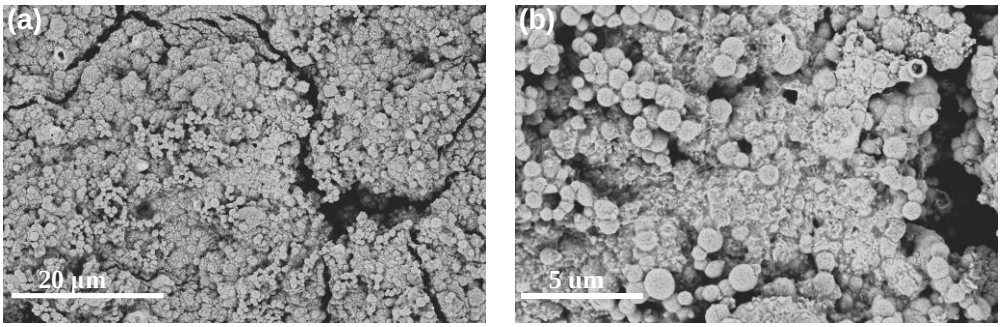

Fig. S15 Low-magnification SEM images of long-cycled electrode at 4 A g^{-1}.

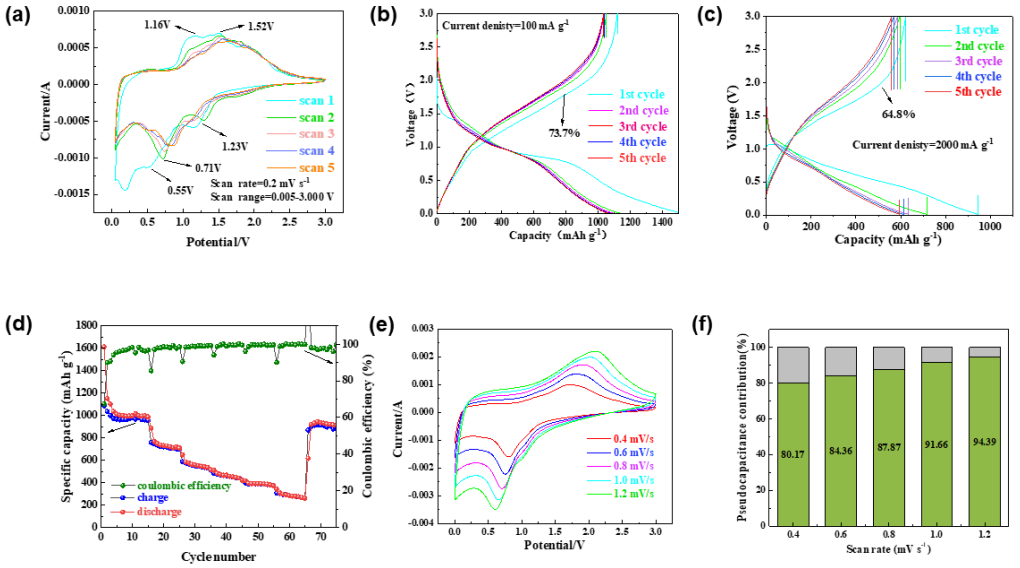

Fig. S16 (a) CV curves at a scan rate of 0.2 mV s^{-1} in the voltage window of 0.005 V-3.0 V vs Li/Li^{+}. Galvanostatic charge–discharge profiles at (b) 100 mA g^{-1} and (c) 2000 mA g^{-1}, (d) Rate capability, (e) CV curves at different scan rates after several cycles, and (f) Corresponding bar chart showing the percent of pseudocapacitive contribution at different scan rates of amorphous $FeCl_3$-MOF-20 electrode. The amorphous $FeCl_3$-MOF-20 electrode shows similar CV curves, as well as similar charge–discharge curve characteristics as Fe (II, III)-MOFs-20 anode at 100 mA g^{-1}. It delivers a high first discharge capacity of 1519.7 mAh g^{-1}, and charge capacity of 1119.2 mAh g^{-1}, respectively with first CE of 73.7%. The first CE at large charge–discharge current (2000 mA g^{-1}) can also approach 64.8%. The slightly lower CE compared with Fe (II, III)-MOFs-20 anode can be ascribed to its litter higher BET surface area. Besides, the amorphous $FeCl_3$-MOF-20 electrode also shows relatively good rate performance in limited electrochemical cycles and ultrafast near-pseudocapacitance lithium storage.

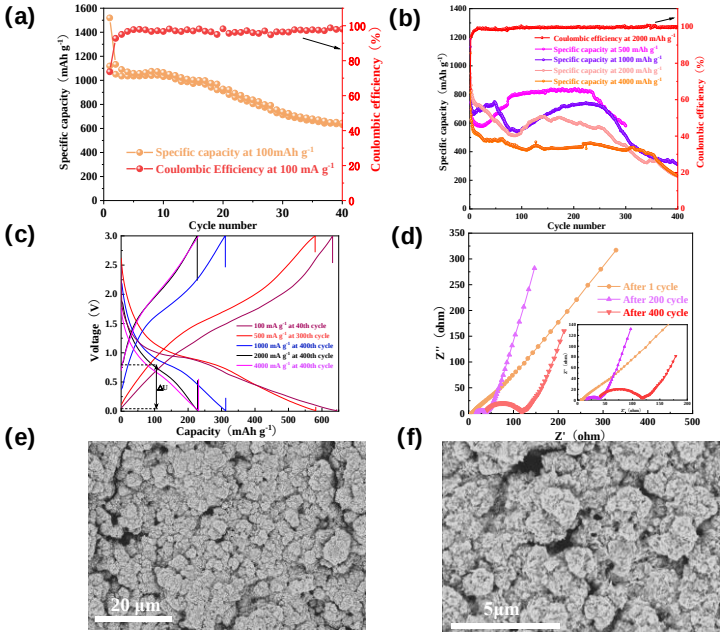

Fig. S17 (a) Cycling performance at a current rate of 100 mA g^{-1}, (b) Cycling performance at high current rates (0.5, 1, 2 and 4 A g^{-1}), (c) Charge-discharge curves at different current density after the cycling test, (d) EIS spectra at 1st/200th/400th cycles with a current density of 1000 mA g^{-1} and (e, f) SEM images of long-cycled electrode at 4 A g^{-1} of $FeCl_3$-MOF-20 electrode. The $FeCl_3$-MOF-20 particles shows rapid capacity decay during the cycling test at various current rates (0.1 ,0.5, 1, 2 and

4 A g^{-1}). The high IR drop ΔU observed after long-term cycling at high rates is consistent with the relatively large increase in impedance associated resistance after long cycling, indicating unstable SEI and more electrolyte reactions, as can also be reflected by the relatively small CE after long cycles. The unstable structure is evidenced by SEM images of the cycled electrode that shows obvious agglomeration and deformation of the spherical particles, demonstrating that the solid spherical structure cannot effectively buffer the volume change during repeated cycling.

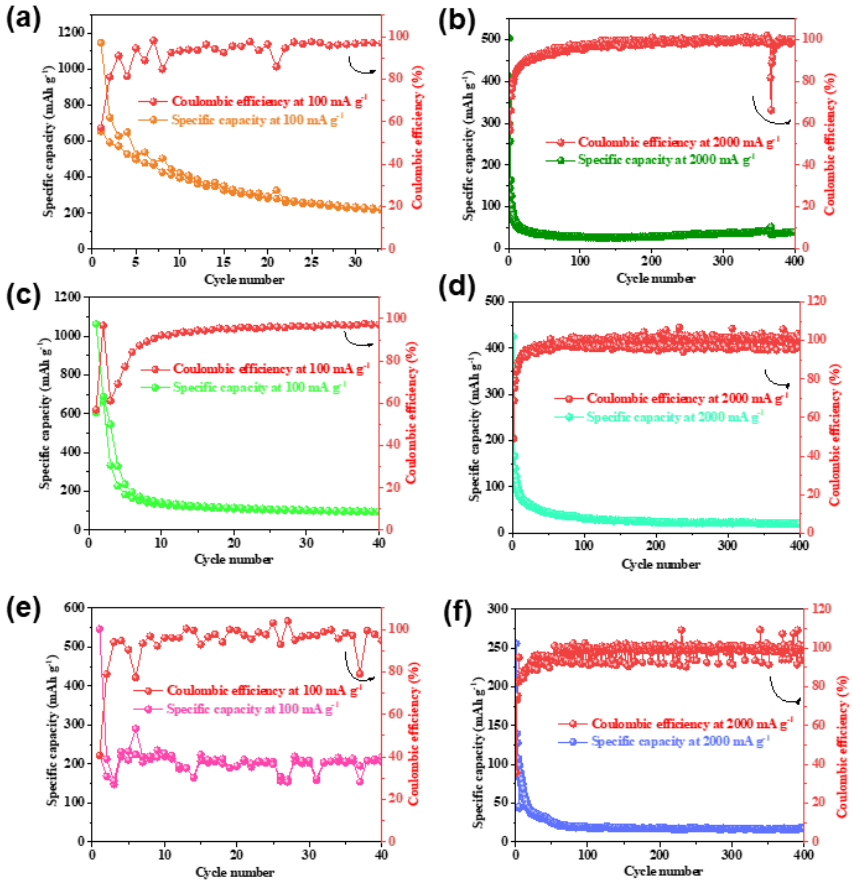

Fig. S18 Electrochemical performance of (a, b) Fe (II, III)-MOFs-40, (c, d) Fe (II, III)-MOFs-60, and (e, f) Fe (II, III)-MOFs-80.

Table S1 Comparison of CE of the first charge/discharge of Fe (II, III)-MOFs-20 with reported MOF anodes.

MOF anode	Initial CE (%)	Current density (mA g^{-1})	References
PCN- 600	49	100	[3]
Fe-MOF/ rGO	43.3	50	[4]
MIL-53 (Fe) @rGO	42.3	100	[5]
Co-BDC	39.75	200	[6]
Co-MOF-74	38	100	[7]
Cu–MOF	44.2	100	[8]
TTFs-Zn-MOF	36.6	200	[9]
Sn-PMA	42.2	200	[10]
Pb-BTC	50	100	[11]
Mg-MOF-74/ Cu	49.6	500	[12]
$[Co_{1.5}L(H_2O)_4]_n$	43.9	372	[13]
CMPS-1	42.7	400	[14]
Fe (II, III)-MOFs-20	81.1/67.1	100/2000	This work

References

1. Ding, J. Wan, Y. Ma, Y. Wang, X. Li, J. Sun and M. Pu, *Chemosphere*, 2021, **270**, 128620.
2. Chen, Y. Wu, X. Han, T. Peng, Q. Qi, H. Sun, X. Hu, Y. Wang, B. Lin, Q. Xiong, Y. Yuan and H. Qin, *ChemistrySelect*, 2023, **8**, e202301281.
3. L. Sun, J. Xie, Z. Chen, J. Wu and L. Li, *Dalton Trans*, 2018, **47**, 9989–93.
4. Y. Jin, C. Zhao, Z. Sun, Y. Lin, L. Chen, D. Wang and C. *Shen, RSC Adv*, 2016, **6**, 30763–8.
5. C. Zhang, W. Hu, H. Jiang, J.-K. Chang, M. Zheng, Q.-H. Wu and Q. Dong, *Electrochim Acta*, 2017, **246**, 528–35.
6. X. Hu, H. Hu, C. Li, T. Li, X. Lou, Q. Chen and B. Hu, *J Solid State Chem*, 2016, **242**, 71–6.
7. J.-J. Song, B. He, X. Wang, Y. Guo, C. Peng, Y. Wang, Z. Su and Q. Hao, *J Mater Sci*, 2021, 5617178–90.
8. Y. Luo, M. Wu, B. Pang, J. Ge, R. Li, P. Zhang, M. Zhou, L. Han and S. Okada, *ChemistrySelect*, 2020, **5**, 4160–4.
9. Y.-G. Weng, W.-Y. Yin, M. Jiang, J.-L. Hou, J. Shao, Q.-Y. Zhu and J. Dai, *ACS Appl Mater Interfaces*, 2020, **12**, 52615–23.
10. S.-B. Xia, L.-F. Yao, H. Guo, X. Shen, J.-M. Liu, F.-X. Cheng and J.-J. Liu, *J Power Sources*, 2019, 440.
11. F. Baskoro, H.-Q. Wong, K.-B. Labasan, C.-W. Cho, C.-W. Pao, P.-Y. Yang, C.-C. Chang, C.-I. Chen, C.-C. Chueh, W. Nie, H. Tsai and H.-j. Yen, *Energy Fuels*, 2021, **35**, 9669–82.
12. X. Li, C. He, J. Zheng, D. Wu, Y. Duan, Y. Li, P. Rao, B. Tang and Y. Rui, *ACS Appl Mater Interfaces*, 2020, **12**, 52864–72.
13. G. Li, H. Yang, F. Li, F. Cheng, W. Shi, J. Chen and P. Cheng, *ACS Inorg. Chem*, 2016, **55**, 4935–4940.
14. H. Fei, X. Liu, Z. Li and W. Feng, *Electrochim Acta,* 2015, **174**, 1088-1095.